Chapter 12
Co-electrospun Brain Mimetic Hollow Microfibres Fibres for Diffusion Magnetic Resonance Imaging

Feng-Lei Zhou, Penny L. Hubbard Cristinacce, Stephen J. Eichhorn, and Geoff J.M. Parker

Abstract Diffusion magnetic resonance imaging (dMRI) provides a non-invasive tool to explore biological tissues, including brain with its highly organised hierarchical fibrous structures. An MR phantom is a test object with known size and material for the calibration of MR scanners and the validation of image processing algorithms. Despite extensive research on the development of brain-mimicking phantoms, there are significant problems with using the existing phantoms for dMRI. This chapter is designed to lead the reader through the development of brain-mimetic phantoms for application in dMRI. Our starting point is a brief introduction to the dMRI technique and phantoms previously developed to mimic brain tissues. The second section focuses on the preparation and characterization of novel physical phantoms composed of co-electrospun hollow microfibres. Finally, the evaluation of the developed co-electrospun phantoms is presented in the third section.

F.-L. Zhou (✉)
Centre for Imaging Sciences, The University of Manchester, Manchester M13 9PT, UK

The School of Materials, The University of Manchester, Manchester M13 9PL, UK

CRUK-EPSRC Cancer Imaging Centre in Cambridge and Manchester, Manchester M20 3LJ, UK
e-mail: fenglei.zhou@manchester.ac.uk

P.L. Hubbard Cristinacce
Centre for Imaging Sciences, The University of Manchester, Manchester M13 9PT, UK

School of Psychological Sciences, University of Manchester, Manchester M13 9PT, UK

S.J. Eichhorn
College of Engineering, Mathematics and Physical Sciences, University of Exeter, Exeter EX4 4QF, UK

G.J.M. Parker
Centre for Imaging Sciences, The University of Manchester, Manchester M13 9PT, UK

CRUK-EPSRC Cancer Imaging Centre in Cambridge and Manchester, Manchester M20 3LJ, UK

12.1 Introduction

12.1.1 Diffusion MRI

Diffusion magnetic resonance imaging (dMRI) is a mature MRI technique, which was introduced in the 1980s but with the first applications realised in the early 1990s [1]. This technique combines a diffusion measurement with MRI and can characterize water diffusion properties at each picture element (pixel) of an image. It therefore provides a non-invasive tool to explore biological tissues, including brain and muscle with their highly organised hierarchical structures characterised by an orientationally anisotropic arrangement in vivo, both in animals and in humans. In these tissues, water does not diffuse equally in all directions, which is often defined as a property called anisotropic diffusion. For example, brain white matter consists of highly ordered bundles at the molecular (filaments), microscopic (axons), and macroscopic (tracts) length scales with orientationally coherent structures often persisting for more than the MRI voxel length scale. Brain water diffuses preferentially along axonal fibre directions but randomly in grey matter (Fig. 12.1).

MRI is the only imaging modality that allows visualization and calculation of molecular diffusion in vivo directly from molecular translational movement of water. Two key parameters as listed below are usually measured in dMRI:

1. Apparent Diffusion Coefficient (ADC): it measures the magnitude of diffusion of water molecules within tissue. The value of ADC is usually expressed in units of $mm^2 \ s^{-1}$ and is lower than free diffusion (and therefore the true diffusion coefficient), and closely reflects tissue microstructure, which impedes water diffusion;
2. Fractional Anisotropy (FA): FA is an index of the degree of alignment across structures and its value ranges from zero (isotropic diffusion, no coherent
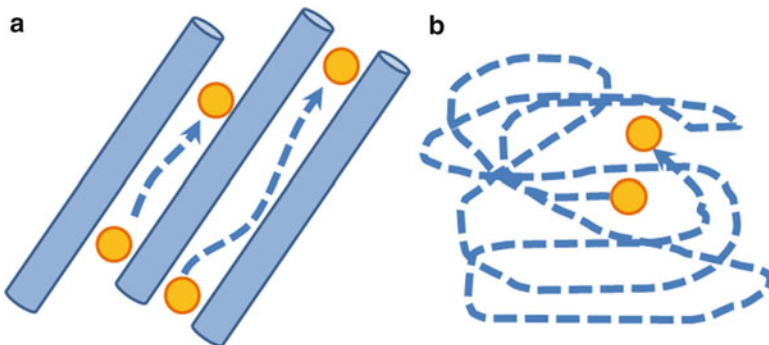

Fig. 12.1 Water diffusion in brain tissue: (**a**) white matter and (**b**) grey matter [2] (©2013 Gracian Garcia-Marti, Angel Alberich-Bayarri, Luis Marti-Bonmati. Originally published in the book edited by Kostas N. Fountas, ISBN 978-953-51-0923-5, under CC BY 3.0 license. Available from: http://dx.doi.org/10.5772/53079)
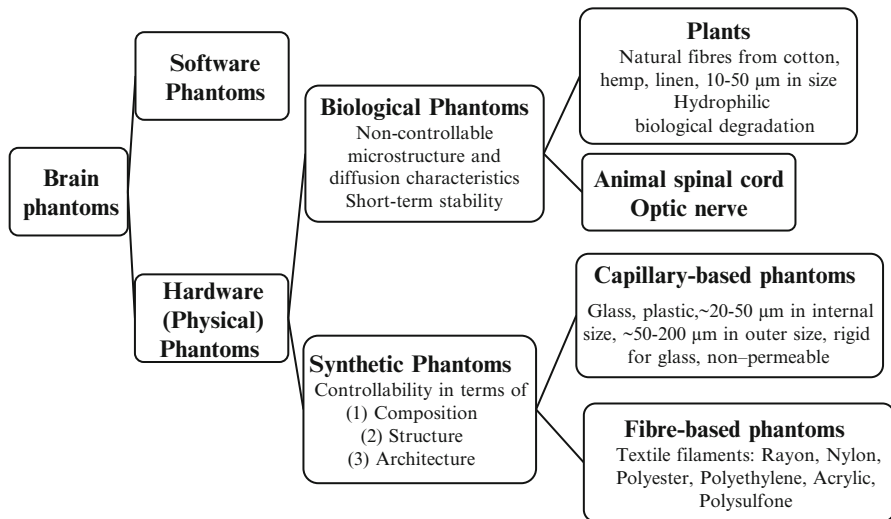
Fig. 12.2 Summary of MR phantom classifications and their characteristics

alignment within the voxel) to one (highly coherent alignment within the voxel). For isotropic water diffusion, the water displacements are equal in every direction and the FA value is zero, whereas diffusion in ordered structures has a higher FA.

12.1.2   MRI Phantoms

12.1.2.1   Imaging Phantoms

Imaging phantoms are artificial objects of known size and composition that are scanned in the area of medical imaging to evaluate the performance of various imaging devices including MRI, CT, Ultrasound, PET, and other modalities. MR phantoms can be a fluid-filled container or tube containing structures of various materials, sizes and shapes, for the calibration of MR scanners and the validation of image processing algorithms. Existing dMRI phantoms have been made from animal tissues, plant stems and textile filaments. Figure 12.2 above summarises imaging phantom classifications and their characteristics.

12.1.2.2   Brain Mimicking Phantoms

Tissue-mimicking phantoms for neurological use have to date proved to be a promising, but limited, tool for calibration and validation of MR scanners and

methods. These phantoms aim to mimic the cellular structure of tissues on the micrometre scale and the long-range connections within the brain on the centimetre scale. It is desirable to have a phantom that exhibits the same or similar properties ("cell" size, "tract" structure, "membrane" permeability, etc.) to human and/or animal tissue, but there are significant problems with using the existing brain phantoms, i.e., the uncontrollable structure of natural phantoms and the large diameters of synthetic phantoms [3, 4].

12.1.2.3 Natural and Synthetic Phantoms

Plant materials and animal tissues have been used as biological phantoms [5–9]. However, they are poor choices for calibration purposes as the exact microstructure and diffusion characteristics of these materials do not closely match with in vivo human tissue, and they are inherently uncontrollable in experimental use and chemically unstable during storage.

Synthetic phantoms of brain white matter are usually made from glass or plastic capillary and textile filament fibres [8, 10–12]. However, glass capillaries are usually rigid and plastic capillaries have larger diameters than typical axons, which limits the macroscopic and microscopic geometry of phantom design. All these available textile filament fibres (see Fig. 12.3) are solid, and none of existing synthetic options have non-negligible and tuneable membrane permeability. It also remains a challenge to regulate the angular distribution of fibres and construct complex fibre geometries such as crossing, kissing or branching present in brain tissue. As a result, the dissimilarity between the microscopic geometry of the existing phantoms and that of brain tissue sets a limit on the degree of validation that they can provide and, to date, has necessitated the use of live animal studies in which the measured diffusion characteristics can be validated against tract tracer methods and post-mortem histology.
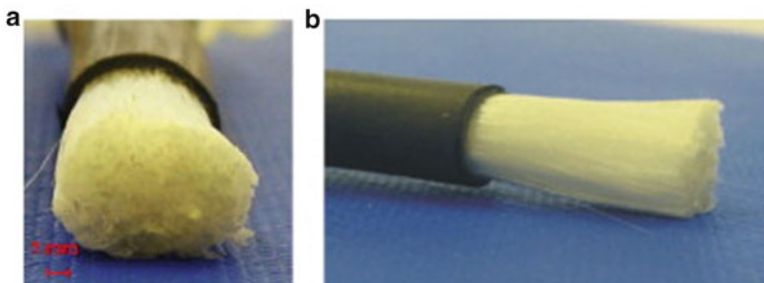

Fig. 12.3 Photographs of a fiber phantom with the shrinking tube partly removed: (**a**) transversal; (**b**) longitudinal view (Reprinted with permission from [8]. Copyright (2008) Elsevier)

12.2   Hollow Microfibres by Co-electrospinning

12.2.1   Co-electrospinning

Electrospinning is a technique employing electrostatic forces to preparing polymeric fibres having diameters in the range of around 100 nm to a few microns from polymer solutions or melts. As a modified process, co-electrospinning (co-ES) can be used to fabricate polymeric fibres with unique core–sheath or hollow structures. Figure 12.4a depicts a schematic of the co-electrospinning process. In coaxial electrospinning, one of the key components lies in its spinneret, consisting of two concentric needles with one located inside another (Fig. 12.4b). A DC high voltage is applied to the spinneret, and it deforms the compound droplet. A compound jet is generated on the tip of the deformed droplet, and in an ideal case, a core–shell or hollow nano/microfibre is created (Fig. 12.4c). In order to obtain a stable compound jet, there are a few general features for designing a coaxial spinneret: (1) better concentricity of the inner and outer needles; (2) controllable flow rates for both the inner and outer solutions, respectively; (3) adjustable protruding length of the inner needle along the axis; and (4) changeable tubular gap between the needle tip openings (see right bottom of Fig. 12.4b).

12.2.2   Co-ES Hollow Microfibres

12.2.2.1   Random Hollow Microfibres

Random hollow microfibres are straightforward produced on a static grounded fibre collector in the co-ES process due to its inherent jet trajectory comprised of straight and spiral sections. Optical and electron microscopes are widely used tools to characterize
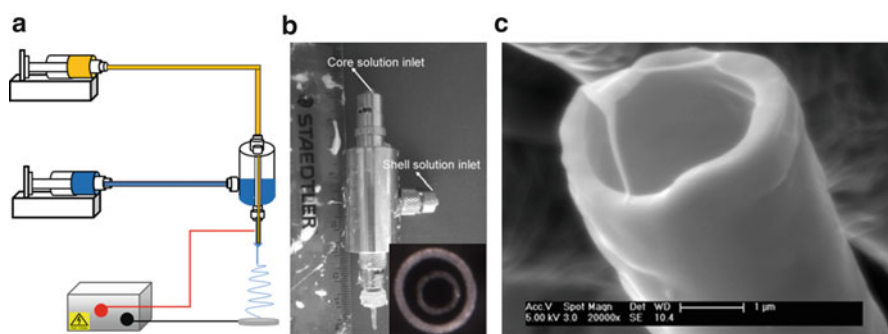

Fig. 12.4 (**a**) Schematic of a co-electrospinning process; (**b**) A spinneret for coaxial electrospinning used in our laboratory (*inlet*: spinneret tip); (**c**) SEM micrograph of cross-section of one hollow fibre by coaxial electrospinning
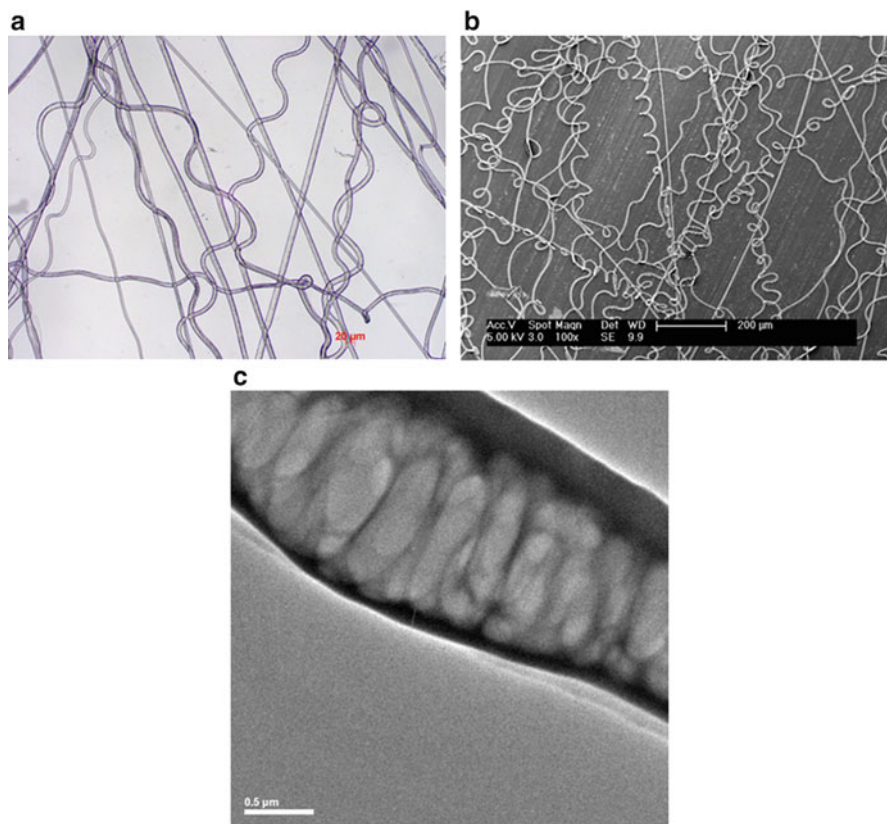
Fig. 12.5 (**a**) Optical image of co-ES polycaprolactone(shell)/polyethylene oxide (core) microfibres (9.0 and 3.0 mL h^{-1} shell and core flow rates, 11.4 kV applied voltage, 12.0 cm working distance); (**b**) SEM image of co-ES polycaprolactone(shell)/polyethylene oxide (core) microfibres (5.0 and 0.2 mL h^{-1} shell and core flow rates, 18.0 kV applied voltage, 20.0 cm working distance); (**c**) TEM image of co-ES polycaprolactone(shell)/sugar (core) microfibres (1.0 and 0.1 mL h^{-1} shell and core flow rates, 9 kv applied voltage, 10.0 cm working distance)

the surface morphology of the resultant co-ES hollow microfibres. Typical optical and scanning electron microscope (SEM) images of the surface morphology of a random co-ES hollow microfibre mesh are shown in Fig. 12.5a–b. In order to confirm the core-shell structures, a transmission electron microscope (TEM) is often used, as shown in Fig. 12.5c, revealing the sugar-polycaprolactone core-shell structured fibre.

To date, four different combinations of core-shell materials (two categories: polymer-polymer and non polymer-polymer) have been successfully used to produce hollow microfibres in our recent studies. SEM, together with freeze fracture, is very useful to examine the cross-sectional morphology of co-ES fibres. The cross-sections of these co-ES fibre meshes are presented in Fig. 12.6, from which cross-sectional pore sizes and distributions can be measured. In general, in order to obtain a stable co-ES and thus well-defined core-shell fibre structure, it is necessary for
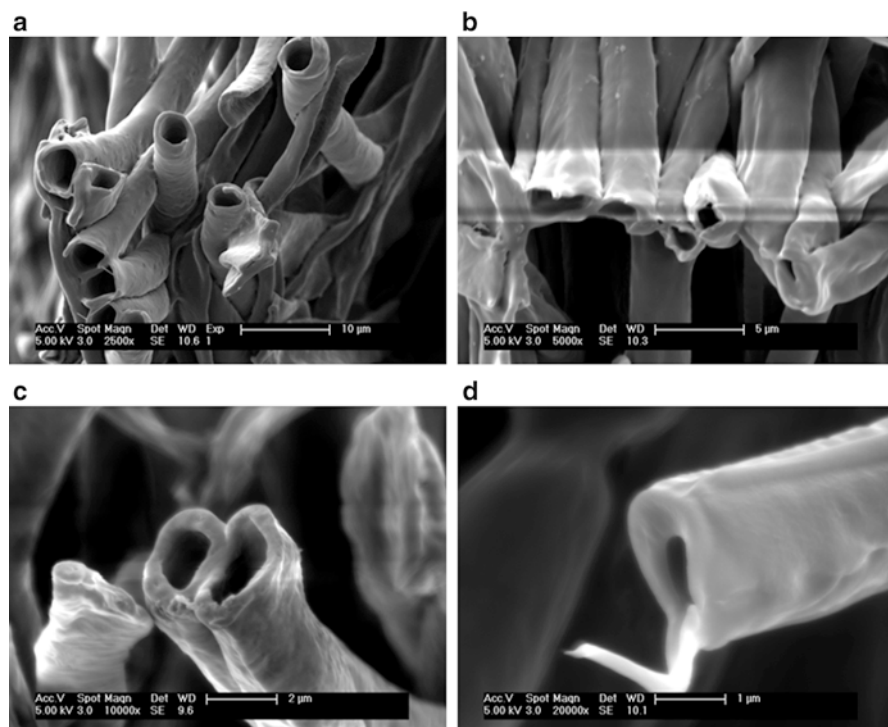
Fig. 12.6 SEM images of cross-sections of co-ES hollow microfibre meshes from (**a**) PCL shell – PEO (polyethylene oxide) core; (**b**) PCL shell – olive oil core; (**c**) PCL shell – mineral oil core; (**d**) PCL shell – sugar aqueous solution core

shell materials to have good fibre spinnablity (e.g., polycaprolactone (PCL) used in our study) and for core materials (e.g., polymer solutions preferably, olive oil, mineral oil or sugar solution) to be sufficiently viscous to withstand high stretching forces exerted on the core fluid. More interestingly, inner diameters (I.D.s) of hollow microfibres can be tuned by both co-ES process parameters (i.e. core solution flow rate) and core-shell solution materials. Figure 12.7 shows a few typical co-ES hollow microfibres with different sizes ranging from ~1 to ~12 μm. Most recently, random hollow microfibres have been successfully used to mimic brain grey matter [13].

12.2.2.2 Aligned Hollow Microfibre Bundles and Strips

Aligned hollow microfibre bundles have been produced by co-electrospinning of PCL shell and PEO core by using a rotating collector as shown in Fig. 12.8. In our recent studies, extensive efforts have been devoted to the exploration of the values of the electric field and core-shell flow rates in order to obtain their operating
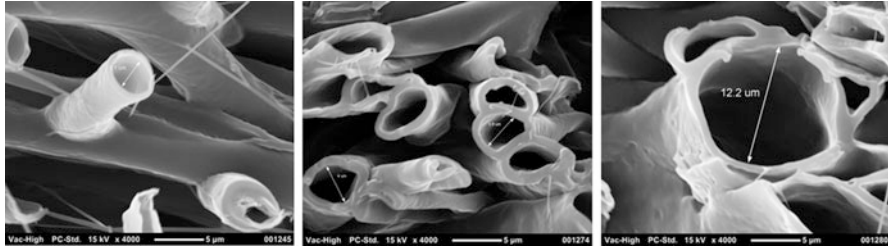
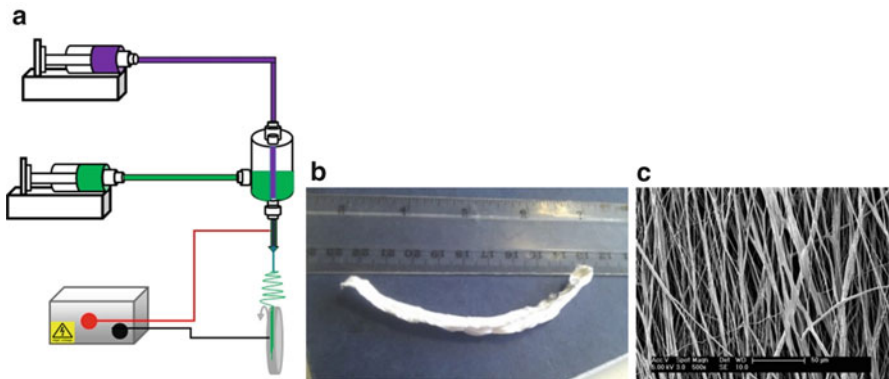**Fig. 12.7** SEM images of co-ES hollow PCL shell – PEO core microfibre meshes with various inner diameters

Fig. 12.8 (**a**) Schematic of co-ES process for production of aligned hollow fibre bundle; (**b**) Photo of fibre bundle; and (**c**) SEM image showing surface morphology of fibre bundle

diagrams, where a stable co-ES process could be achieved to produce an effective phantom material [4]. Within the operating diagrams, the core flow rate of PEO solution was adjusted to produce hollow PCL fibres with various inner diameters, while the PCL shell flow rate was maintained constant, since the inner diameter of hollow PCL fibres is expected to be one of key factors affecting the diffusion of the solvent in dMRI.

SEM images in Fig. 12.9a–h reveal that the inner diameters of PCL fibres increased from ~3.3 to ~10.2 µm (Fig. 12.9i) as the core flow rate increased from 0.1 to 2 mL h^{-1}, when the shell flow rate was maintained at 3 mL h^{-1}. There was a similar tendency for the effect of core flow rate when the shell flow rate was increased to 6 mL h^{-1} (Fig. 12.9j). As shown in Fig. 12.9i, the reproducibility of the inner diameters of eight hollow PCL samples produced using different core flow rates was good. Based on these results, the inner diameters of the PCL fibres were easily adjusted to suit the application of axon-mimicking phantoms, by fine-tuning the core-shell flow rates. Compared with the effect of the core flow rate, it can clearly be seen from Fig. 12.9k that the shell flow rate had a less significant impact on the inner diameter of co-ES hollow PCL fibres. This finding was in line with previous reports by Zussman et al. [14, 15]. However, it must be pointed out that the
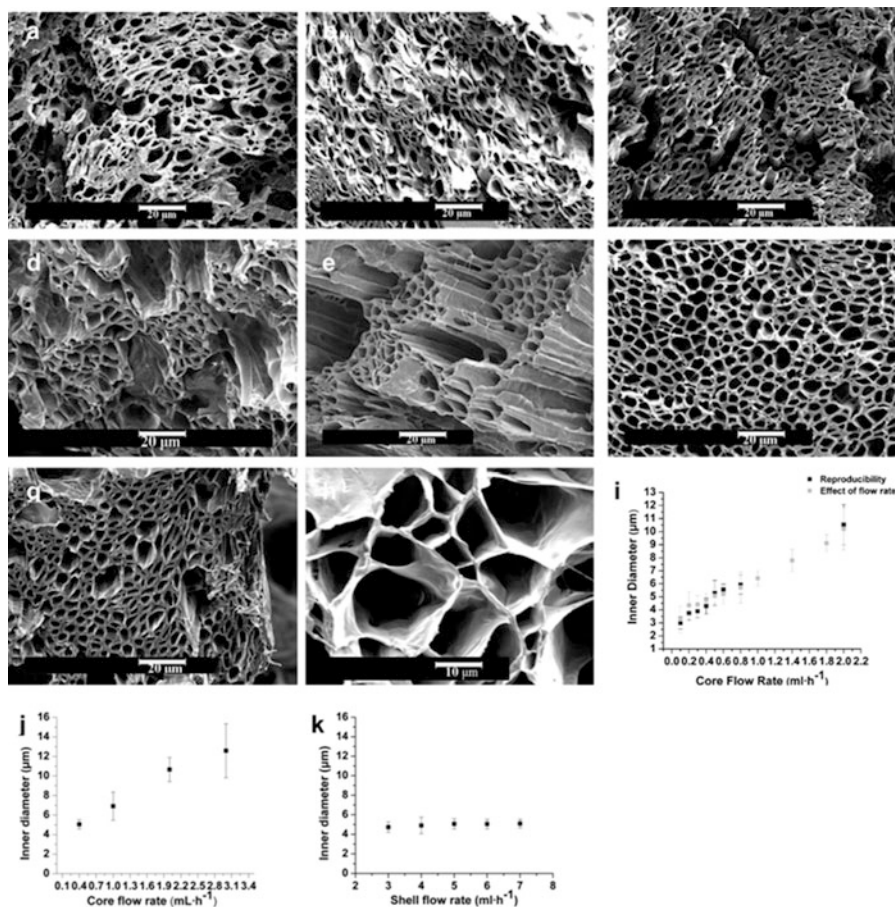
Fig. 12.9 SEM images of hollow PCL fibres produced at different core flow rates: (**a**) 0.1; (**b**) 0.2; (**c**) 0.3; (**d**) 0.4; (**e**) 0.5; (**f**) 0.6; (**g**) 0.8; (**h**) 2 mL h^{-1}; (**i**) the relationship between the inner diameter of hollow PCL fibres and core flow rate at a 3 mL h^{-1} shell flow rate, showing good reproducibility; (**j**) the relationship between the inner diameter of hollow PCL fibres and PEO core flow rate at 6 mL h^{-1} shell flow rates; (**k**) the relationship between the inner diameter of hollow PCL fibres and shell flow rate. Experimental parameters: 9 kV applied voltage, 5 cm working distance, 3 mL h^{-1} PCL shell flow rate (Reprinted with permission from [4], Copyright (2012) American Chemical Society)

range of shell flow rates used in our studies had to be narrow in order to maintain the stability of the co-ES process, whereas the core flow rate and electric field were fixed.

Another form of aligned hollow microfibre assembly – fibre strip has been also prepared from PCL shell and PEO core with core flow rates of 0.8, 1.4, and 2.0 mL h^{-1} by using a rotating drum mounted on an *x-y* translation stage, as shown in Fig. 12.10. Using the SEM images in Fig. 12.11a–c the area-weighted mean inner diameters of the fibres in the three strips are found to be 9.5, 11.9, and
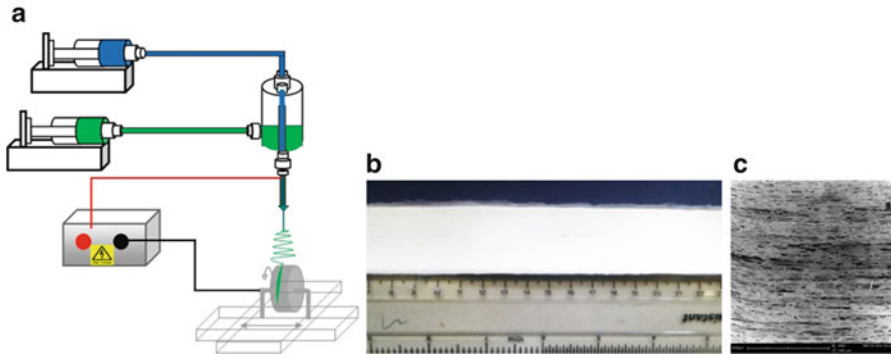
Fig. 12.10 (**a**) schematic of co-ES process for production of aligned hollow fibre strip; (**b**) photo of fibre strip; and (**c**) SEM image showing surface morphology of fibre strip
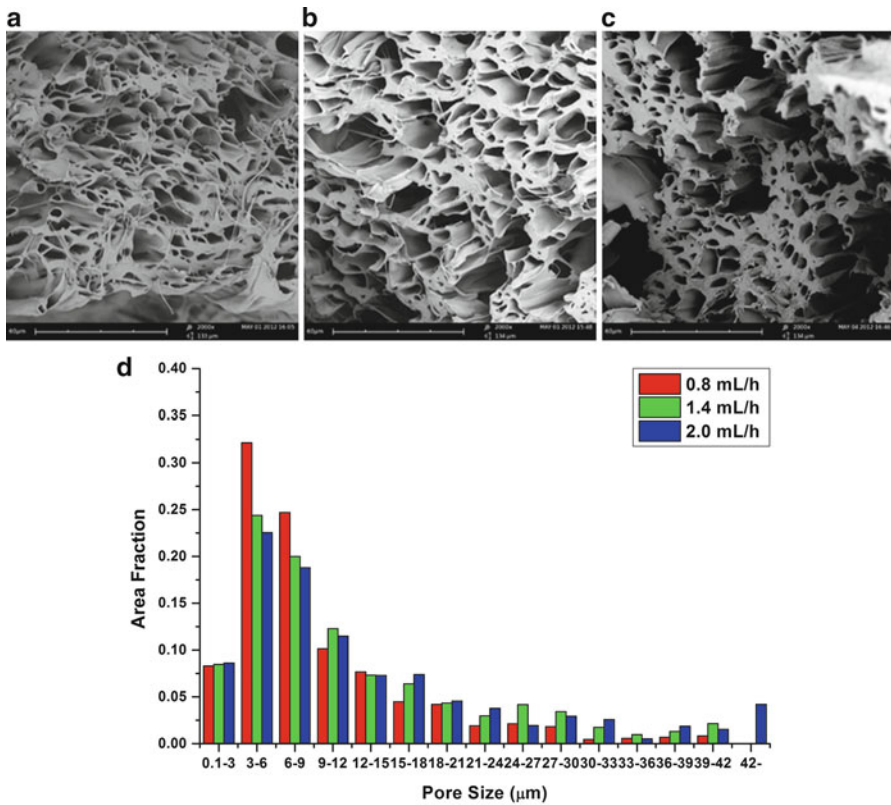

Fig. 12.11 Electron micrographs of co-ES hollow fibre strips produced using the core flow rate of (**a**) 0.8 mL h^{-1}, (**b**) 1.4 mL h^{-1}, (**c**) 2.0 mL h^{-1}, (**d**) A histogram of the area-weighted mean pore size measurements for each strip. (Reprinted with permission from [17]. Copyright (2015) John Wiley and Sons)

13.4 μm, respectively. Figure 12.11d shows the range of inner diameters for each of these strips as a normalized histogram. There is a broad range of fibre inner diameters within the strip, reminiscent of real tissue [16], but it is clear that the mean diameter tends towards higher values for the strips prepared with higher core flow rates. In order to investigate the reproducibility of co-ES hollow microfibres, five strips were prepared with an inner flow rate of 0.8 mL h^{-1}. Figure 12.12 shows
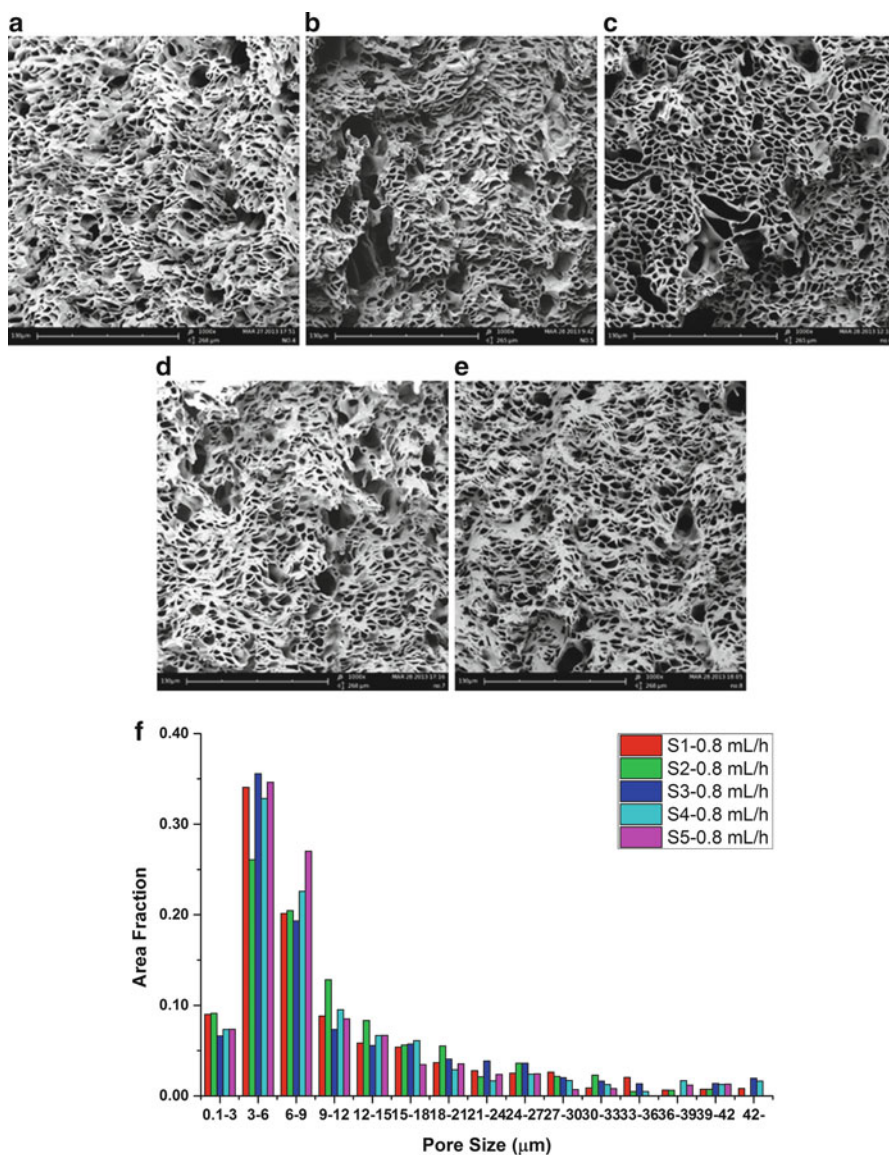

Fig. 12.12 (**a–e**) Representative electron micrographs of five co-ES hollow fibre strips reproducibility using 0.8 mL h^{-1} core flow rate, and (**f**) the histogram of their inner diameters

cross-sectional SEM images with ×1,000 magnification through a strip, cut perpendicular to the axis of the fibres, revealing a microporous structure. Using the SEM images the range of inner diameters for each of these strips is shown as a normalised histogram (Fig. 12.12f).

12.3 Co-ES Microfibre Phantoms and MR Evaluation

Two types of MR phantoms have been developed using co-ES hollow microfibres, which are fibre-bundle based and fibre-strip based, as shown in Fig. 12.13.

12.3.1 Fibre Bundle Based MR Phantoms

MR phantoms were constructed by inserting fibre bundles into MR test tubes, with the fibres aligned along the axis of the tubes. The tubes were filled with the diffusion model liquid, cyclohexane, which is a proton rich solvent capable of infusing into the hydrophobic polymer, with a suitable MRI properties to mimic the free liquid in axonal bodies. Figure 12.14a shows the fibres packed in a glass tube filled with cyclohexane. In dMRI, MR signal is sensitive to the molecular diffusion of

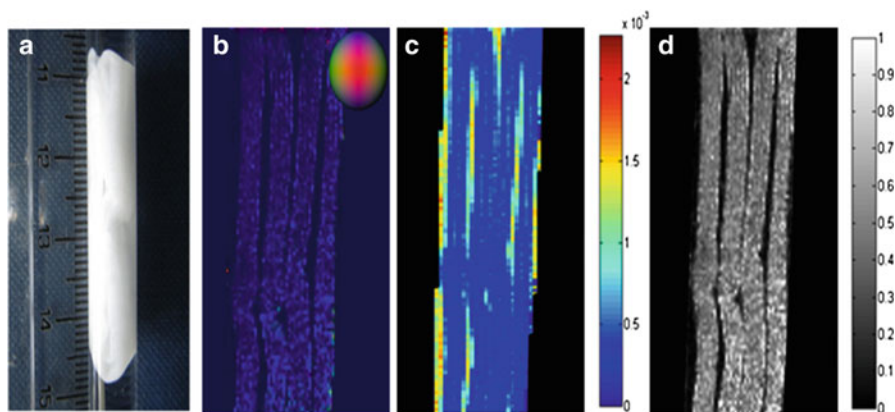**Fig. 12.13** (**a**) Fibre bundle-based MR phantom; (**b**) Fibre strip-based MR phantom

Fig. 12.14 (**a**) Fibre phantoms in a glass tube filled with solvent, cyclohexane; (**b**) Single slice through the phantom, revealing the consistent preferential alignment of the micrometre-scale fibre along the axis of the tube; (**c**) A mean diffusivity map revealing lower values in the phantom compared with the free solvent; (**d**) A fractional anisotropy map showing that diffusion within the phantom is anisotropic (approaching 1) and in the solvent is isotropic (approaching 0). (Reprinted with permission from [4]. Copyright (2012) American Chemical Society)

cyclohexane and can change when the free diffusive passage of these solvent molecules is restricted or hindered by surrounding barriers. The measurement of ADC in multiple directions allows us to determine the orientation of these barriers. Due to the anisotropic structure, the least hindered diffusion (or highest diffusion coefficient) in the hollow aligned co-ES fibre bundles is expected to be parallel to the fibre alignment direction. Figure 12.14b shows a colour map of the orientation of the least restricted diffusion and, therefore, the principal direction of the fibres in the bundles as anticipated from the construction of the phantom. The colour key ball in the figure reveals that fibres in red run into and out of the page, in green run from left to right, and in blue run up and down. The figure clearly shows the principal direction of the aligned fibres to be along the axis of the tube.

Figure 12.14c shows the mean diffusivity (MD) of cyclohexane in the hollow microfibres, revealing that the average parallel and perpendicular apparent diffusion coefficients are significantly lower than that for free cyclohexane. Figure 12.14d shows the fractional anisotropy (FA). The MD value in the our study is higher and FA value lower than the average MD and FA values of the ex vivo optic nerve of a rat, respectively, measured by Richardson et al. [18]. These values are, however, in the approximate in vivo biological range for white matter [19]. Considering the fact that the average diameter of hollow microfibres in the phantom is $10.2 \pm 1.6 \, \mu m$, which is consistent with large axons in white matter [20], the MD value is expected to be a little higher and FA value a little lower than in the optic nerve. These ex vivo MD and FA values of the optic nerve are however respectively lower and higher than what is generally observed in tissue in vivo. It is worth noting that the phantom sample testing temperature in our study is relatively low (22 °C vs body temperature in the Richardson study), suggesting that the

factors including the use of cyclohexane as a solvent and the relative lack of microstructural complexity in the phantom when compared with biological tissue may also influence the parameter values.

12.3.2 Fibre Strip-Based MR Phantoms

A similar procedure as described in Sect. 12.3.1 has been followed to prepare MR phantoms using strips with difference fibre diameters (Fig. 12.15a). Diffusion tensor imaging (DTI) has been carried out on a Bruker 7 T horizontal bore magnet (Bruker Biospin, Germany).

The FA and the radial diffusivity calculated from diffusion-tensor images are plotted against the area-weighted mean inner diameters measured from SEM images. As shown in Fig. 12.15b–c, the radial diffusivity increases with the increasing mean inner diameter of the fibres, whereas FA decreases linearly. This trend is expected as, dependent on the diffusion time of the acquisition, an increase in inner diameter reduces the restriction to the diffusion of cyclohexane molecules perpendicular to the axis of the fibres. This leads to a subsequent decrease in FA: from 0.45 ± 0.05 to 0.33 ± 0.04, and increase in the measured apparent diffusion coefficient perpendicular to the fibres from $0.38 \pm 0.05 \times 10^3$ cm s^{-1} to $0.61 \pm 0.06 \times 10^3$ cm s^{-1}.

We have carried out a study investigating whether the phantoms prepared under the same co-ES conditions could lead to a reproducible dMRI signal. Five fibre strips prepared in the Sect. 12.2.2.2 using an inner flow rate of 0.8 mL h^{-1} (see Fig. 12.12) and were then prototyped into five phantoms. These phantoms were scanned concurrently on a 3 T clinical scanner using the manufacturer's high
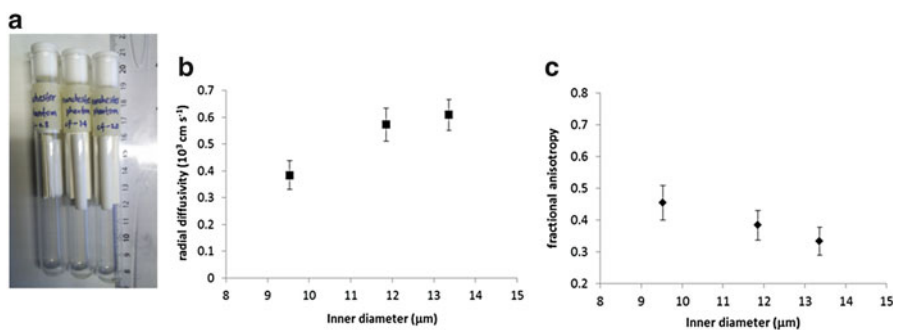

Fig. 12.15 (**a**) Three tubes containing phantoms with fibers of increasing inner diameter; (**b**) area-weighted mean pore inner diameter (measured from SEM) against fractional anisotropy (measured from DTI); (**c**) area-weighted mean pore inner diameter against radial diffusivity (Error bars are standard deviations from the mean; Reprinted with permission from [17]. Copyright (2014) John Wiley and Sons)

resolution DTI protocol. The results of both the SEM and DTI have shown that there is only a small amount of variation between the samples (see details in [17]).

A final point of consideration for a useful phantom material is the long-term stability of the fiber material in the diffusion solvent. It is important that the material does not degrade or change structure within a reasonable time window. Short-term stability of PCL fibres in cyclohexane has been shown to be good over both a 1-week [4] and 12-month period, but further study of the long term stability is desirable.

12.4   Conclusions

In summary, we have developed a novel brain white matter mimicking phantom comprising co-ES hollow polymeric fibres, which can be constructed and used as reference materials for diffusion magnetic resonance imaging. The inner diameter of co-ES hollow fibres can be tuned by controlling the core flow rate and core-shell solution pairs in order to provide structures with similar inner diameters to axon fibres in brain white matter. Our study has demonstrated that the developed phantoms can mimic the cellular barriers imposed by axonal cell membranes and myelin, and can result in expected responses (ADC and FA values) of MR scanner by changing their size. The developed phantoms are reproducible and have been tested in other imaging centres in the UK, EU and US. Research in this area can potentially enable the development of biomimetic phantoms that can mimic a range of biological structures within the body, potentially providing substitutes for animal tissues, and allowing the stable and reproducible validation and calibration of diffusion MRI in other organs and cellular structures.

References

1. S. Mori, P.B. Barker, Diffusion magnetic resonance imaging: its principle and applications. Anat. Rec. **257**(3), 102–109 (1999). doi:10.1002/(sici)1097-0185(19990615)257:3<102::aid-ar7>3.0.co;2-6
2. G. García-Martí, A. Alberich-Bayarri, L. Martí-Bonmatí, Brain structure MR imaging methods: morphometry and tractography. Nov. Front. Adv. Neuroimaging (2013). doi:10.5772/53079
3. H. Johansen-Berg, T.E.J. Behrens (eds.), *Diffusion MRI: From Quantitative Measurement to In-Vivo Neuroanatomy The Validation of Tractography* (Academic, Amsterdam, 2009)
4. F.-L. Zhou, P.L. Hubbard, S.J. Eichhorn, G.J.M. Parker, Coaxially electrospun axon-mimicking fibers for diffusion magnetic resonance imaging. ACS Appl. Mater. Interfaces **4**(11), 6311–6316 (2012). doi:10.1021/am301919s

5. S. Boujraf, R. Luypaert, H. Eisendrath, M. Osteaux, Echo planar magnetic resonance imaging of anisotropic diffusion in asparagus stems. MAGMA **13**(2), 82–90 (2001). doi:10.1007/bf02668156

6. Y. Assaf, R.Z. Freidlin, G.K. Rohde, P.J. Basser, New modeling and experimental framework to characterize hindered and restricted water diffusion in brain white matter. Magn. Reson. Med. **52**(5), 965–978 (2004). doi:10.1002/mrm.20274

7. M. Descoteaux, E. Angelino, S. Fitzgibbons, R. Deriche, Apparent diffusion coefficients from high angular resolution diffusion imaging: estimation and applications. Magn. Reson. Med. **56**(2), 395–410 (2006). doi:10.1002/mrm.20948

8. E. Fieremans, Y. De Deene, S. Delputte, M.S. Özdemir, Y. D'Asseler, J. Vlassenbroeck, K. Deblaere, E. Achten, I. Lemahieu, Simulation and experimental verification of the diffusion in an anisotropic fiber phantom. J. Magn. Reson. **190**(2), 189–199 (2008). doi:10.1016/j.jmr.2007.10.014

9. P. Pullens, A. Roebroeck, R. Goebel, Ground truth hardware phantoms for validation of diffusion-weighted MRI applications. J. Magn. Reson. Imaging **32**(2), 482–488 (2010). doi:10.1002/jmri.22243

10. C. Poupon, B. Rieul, I. Kezele, M. Perrin, F. Poupon, J.-F. Mangin, New diffusion phantoms dedicated to the study and validation of high-angular-resolution diffusion imaging (HARDI) models. Magn. Reson. Med. **60**(6), 1276–1283 (2008). doi:10.1002/mrm.21789

11. P. Fillard, M. Descoteaux, A. Goh, S. Gouttard, B. Jeurissen, J. Malcolm, A. Ramirez-Manzanares, M. Reisert, K. Sakaie, F. Tensaouti, T. Yo, J.-F. Mangin, C. Poupon, Quantitative evaluation of 10 tractography algorithms on a realistic diffusion MR phantom. NeuroImage **56**(1), 220–234 (2011). doi:10.1016/j.neuroimage.2011.01.032

12. E. Fieremans, Y.D. Deene, S. Delputte, M.S. Özdemir, E. Achten, I. Lemahieu, The design of anisotropic diffusion phantoms for the validation of diffusion weighted magnetic resonance imaging. Phys. Med. Biol. **53**(19), 5405 (2008)

13. A. Ye, P.L. Hubbard Cristinacce, F.-L. Zhou, Z. Yin, G.J.M. Parker, R. Magin, Diffusion tensor MRI phantom exhibits anomalous diffusion. *The Proceeding of The 36th Annual International IEEE EMBS Conference*, Chicago, IL, USA, 26–30 August 2014, pp. 746–749

14. A. Arinstein, R. Avrahami, E. Zussman, Buckling behaviour of electrospun microtubes: a simple theoretical model and experimental observations. J. Phys. D. Appl. Phys. **42**(1), 015507 (2009)

15. S.N. Reznik, A.L. Yarin, E. Zussman, L. Bercovici, Evolution of a compound droplet attached to a core-shell nozzle under the action of a strong electric field. Phys. Fluids **18**(6), 062101 (2006). doi:10.1063/1.2206747

16. Y. Assaf, T. Blumenfeld-Katzir, Y. Yovel, P.J. Basser, Axcaliber: a method for measuring axon diameter distribution from diffusion MRI. Magn. Reson. Med. **59**(6), 1347–1354 (2008). doi:10.1002/mrm.21577

17. P.L. Hubbard, F-L. Zhou, S.J. Eichhorn, G.J.M. Parker, Biomimetic phantom for the validation of diffusion magnetic resonance imaging. Magn. Reson. Med. **73**(1), 299–305 (2015). doi:10.1002/mrm.25107

18. S. Richardson, B. Siow, A.M. Batchelor, M.F. Lythgoe, D.C. Alexander, A viable isolated tissue system: a tool for detailed MR measurements and controlled perturbation in physiologically stable tissue. Magn. Reson. Med. **69**(6), 1603–1610 (2013). doi:10.1002/mrm.24410

19. D.K. Jones, Studying connections in the living human brain with diffusion MRI. Cortex **44**(8), 936–952 (2008). doi:10.1016/j.cortex.2008.05.002

20. J.A. Perge, J.E. Niven, E. Mugnaini, V. Balasubramanian, P. Sterling, Why do axons differ in caliber? J. Neurosci. **32**(2), 626–638 (2012). doi:10.1523/jneurosci. 4254-11.2012